Title

Comparison of odor responses of homologous medial and lateral glomeruli mapped in the olfactory bulb of the mouse

Abbreviated title

Functional imaging of medial/lateral glomeruli

Author names and affiliations

Tokiharu Sato[1, 2], Ryota Homma[1], Shin Nagayama[1]

[1]Department of Neurobiology and Anatomy, McGovern Medical School at the University of Texas Health Science Center at Houston, Houston, TX 77030, USA

[2]Department of System Pathology for Neurological Disorders, Brain Research Institute, Niigata University, Niigata 951-8585, Japan

Correspondence should be addressed to

Shin Nagayama

P.O. Box 20708

Houston, TX 77225-0708

Shin.Nagayama@uth.tmc.edu

Impact Statement

This study used *in vivo* calcium imaging to document the odor-evoked responses in paired glomeruli, demonstrating that activation in medial glomeruli more strongly impacts respiratory-linked odor processing.

Funding

S.N. is supported by NIH/NIDCD grant R01DC013802.

Competing interests

All authors declare no conflicts of interest.

Author contributions

TS, Conceptualization, Data curation, Formal analysis, Writing—original draft, Writing—review and editing; RH, Methodology, Formal analysis, Writing—review and editing; SN, Conceptualization, Supervision, Writing—original draft, Writing—review and editing

Abstract

Olfactory sensory neurons expressing same-type odorant receptors typically project to a pair of glomeruli in the medial and lateral sides of the olfactory bulbs (OBs) in rodents. However, their functional properties remain unclear, because the majority of medial glomeruli are hidden in the septal OB. Recently, trace amine-associated odorant receptors were identified that project to a pair of glomeruli uniquely located in the dorsal OB. We measured the odorant-induced calcium responses of these glomeruli simultaneously and found that they exhibited similar temporal response patterns. However, the medial glomeruli had significantly larger respiration-locked calcium fluctuations than the lateral glomeruli. This trend was observed with/without odorant stimulation in postsynaptic neurons but not in presynaptic sensory axon terminals. This indicates that the medial rather than the lateral OB map enhances the respiration-locked rhythm and transfers this information to higher brain centers.

Introduction

Parallel processing of multiple streams of information improves the speed of processing and provides redundancy for fail-safe operations. Biological parallel streams of information in the brain are not typically identical neuronal circuits but have unique as well as common properties (Kandel et al., 2013). How the brain organizes the distinct processing streams and combines them is not well understood.

Odor information is represented as spatial/temporal glomerular activity patterns on the surfaces of the olfactory bulbs (OBs). In rodents, olfactory sensory neurons (OSNs) expressing the same types of odorant receptors, among ~1,000 repertoires (Buck, 1996), convert chemical signals into electrical signals in a respiratory rhythm and project to approximately two glomeruli in the OB: one on the medioventral side and the other on the dorsolateral side. The axons of these OSN projections traverse the medial/septal and lateral surfaces of the OBs, respectively. Because the two homologous glomeruli are arranged symmetrically in the OB, odor information is represented and processed in two mirror maps (Mombaerts et al., 1996; Nagao et al., 2002, 2000; Zapiec and Mombaerts, 2015). The paired glomeruli are connected via axon collaterals of tufted cells in a point-to-point manner (Belluscio et al., 2002; Lodovichi et al., 2003; Marks et al., 2006). Although the anatomical arrangements of the two maps have been studied, less is known about the functional connections between them (Zhou and Belluscio, 2012, 2008). One pivotal idea is that the complex structure of the olfactory epithelium (OE) affects the sensitivity and timing of odorant responses of OSNs such that a delayed odorant response in one of the maps occurs with low odor concentrations (Kimbell et al., 1997; Schoenfeld and Cleland, 2006; Zhao et al., 2006; Zhou and Belluscio, 2012). The similarity in the spatiotemporal patterns representing odor information between these glomeruli remains unknown, partly because of the

inaccessibility of the medial map, but is essential to understand the features that are common and uncommon between the two streams.

Trace amine-associated receptors (TAARs) were recently recognized as a second group gene family of odorant receptors (Liberles and Buck, 2006). Pairs of OSNs expressing TAARs project to glomeruli in the mediodorsal OB (Dewan et al., 2013; Liberles, 2015; Pacifico et al., 2012; Zhang et al., 2013), which can frequently be observed simultaneously. Moreover, these two glomeruli are functionally identifiable because of their highly selective responses to the specific odorant at a low concentration (Zhang et al., 2013). In the present study, we measured simultaneous odorant responses of these homologous glomerular pairs and compared the response properties between medial and lateral maps. These glomeruli exhibited similar activity patterns of response onset latency, rise and decay times, and amplitudes. However, the medial glomeruli showed significantly larger respiration-locked fluctuations than the lateral glomeruli. The difference was observed in postsynaptic neuronal responses but not presynaptic terminal activity, suggesting that despite similar inputs, the medial map neurons and/or circuits enhance the respiration-locked activity for further odor information processing.

Results

Expression patterns of GCaMP3 in OBs from Cre mouse driver lines.

We recorded odor-evoked neuronal activity in the OBs of mice from multiple transgenic mouse lines. To express the genetically encoded calcium indicator GCaMP3 (Tian et al., 2009) in different types of neurons in the OB, we used four Cre recombinase (Cre)-driver mouse lines. Specifically, OMP-Cre (Li et al., 2004), Gad2-Cre (Taniguchi et al., 2011), DAT-Cre (Bäckman et al., 2006), and Pcdh21-Cre (Nagai et al., 2005) mouse lines were crossed with a Cre-inducible GCaMP3 reporter mouse line (Ai38) (Zariwala et al., 2012) so that GCaMP3 was expressed in OSNs and GABAergic, dopaminergic, and mitral/tufted cells, respectively. We first verified the GCaMP3 expression pattern in each of the Cre-driver mouse lines (Fig. 1 A–D). In OMP-Cre mice, GCaMP3 signals were clearly detected only in OSNs in the glomerular layer (GL) (Fig. 1A). Consistent with a previous report (Wachowiak et al., 2013), GCaMP3 in Gad2-Cre mice was strongly expressed in the external plexiform layer (EPL) and in the granule cell layer (GCL); the expression was predominantly by granule cells, but enhanced detection methods also revealed expression by periglomerular cells in the GCL (Fig. 1B). In DAT-Cre mice, GCaMP3 signals were mostly restricted to the GL (Fig. 1C). High magnification of this layer indicated that GCaMP3 was expressed by juxtaglomerular cells, which were considered to be short-axon (SA) cells (Kiyokage et al., 2010) (inset of Fig. 1C). This pattern of expression was similar to that in the TH (tyrosine hydroxylase)-Cre line, another driver line for expression in dopaminergic cells (Wachowiak et al., 2013). In Pcdh21-Cre mice, GCaMP3 was specifically expressed in mitral/tufted cells, as GCaMP3 signals appeared in somata and neurite processes in superficial EPL and the mitral cell layer (MCL) (Fig. 1D), as reported previously (Huang et al., 2013;

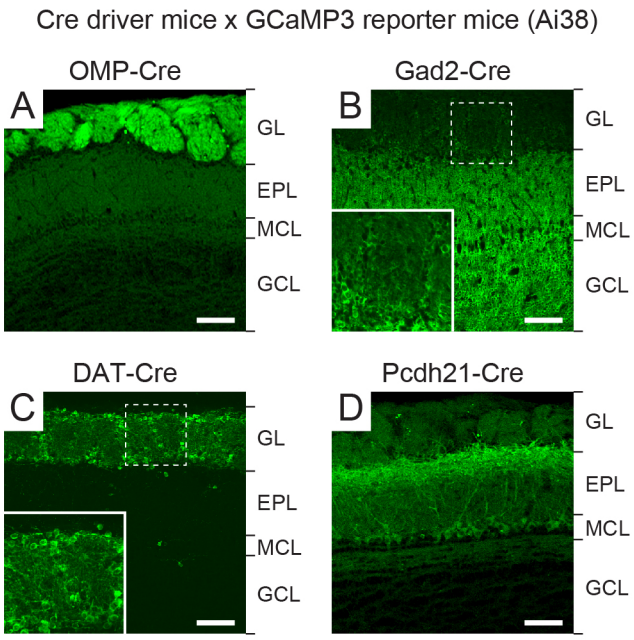

Figure 1: Cell-type-specific expression of GCaMP3 in OBs of mice from different transgenic lines. (A–D) Confocal images of OBs in Cre-dependent GCaMP3 reporter mice crossed with OMP-Cre (A), Gad2-Cre (B), DAT-Cre (C), and Pcdh21-Cre (D) mice. Magnified views of the dashed squares are shown in the insets in B and C. GL, EPL, MCL, and GCL indicate glomerular layer, external plexiform layer, mitral cell layer, and granule cell layer, respectively. Scale bars, 100 μm.

Mizuguchi et al., 2012; Nagai et al., 2005). Although reporter expression is induced in OSNs in another Pcdh21-Cre-driver line (Wachowiak et al., 2013), we did not observe this ectopic expression in our mice. In summary, these Cre mouse lines exhibited the expected cell-type-specific GCaMP3 expression patterns.

Identification of homologous glomeruli in medial and lateral maps.

In vivo optical imaging of the dorsal OB has not been utilized as a means to record activity in the medial map, because most of the glomeruli are located in the medioventral region of the OB (Inaki et al., 2002; Johnson et al., 2009, 2005, 2004, 1999, 1995, Johnson and Leon, 2000, 1996; Mori et al., 2006; Nagao et al., 2000, 2002; Taniguchi et al., 2003; Zapiec and Mombaerts, 2015). However, it was recently demonstrated that OSNs expressing TAARs project to two or a few glomeruli in caudal regions of the dorsal OB (Dewan et al., 2018, 2013; Johnson et al., 2012; Liberles, 2015; Pacifico et al., 2012; Zhang et al., 2013). These medial and lateral glomeruli can easily be identified, because axons from TAAR-expressing OSNs projecting to the dorsomedial glomeruli transverse the anteromedial (septal) surface of the OB, whereas those projecting to the dorsolateral glomeruli transverse the anterolateral surface. The axonal trajectories and odorant response profiles of glomeruli receiving projections from OSNs expressing TAAR3 and TAAR4 are well characterized (Dewan et al., 2018, 2013; Pacifico et al., 2012; Zhang et al., 2013). Specifically, these glomeruli are highly sensitive to isopentylamine (IPA) and phenylethylamine (PEA), respectively. Therefore, we imaged simultaneously these medial and lateral glomeruli that receive input from TAAR3- and TAAR4-expressing OSNs.

Using IPA and PEA at final concentrations of 0.02% and 0.002%, which reliably and specifically induce activation of the glomeruli receiving inputs from TAAR3- and TAAR4-

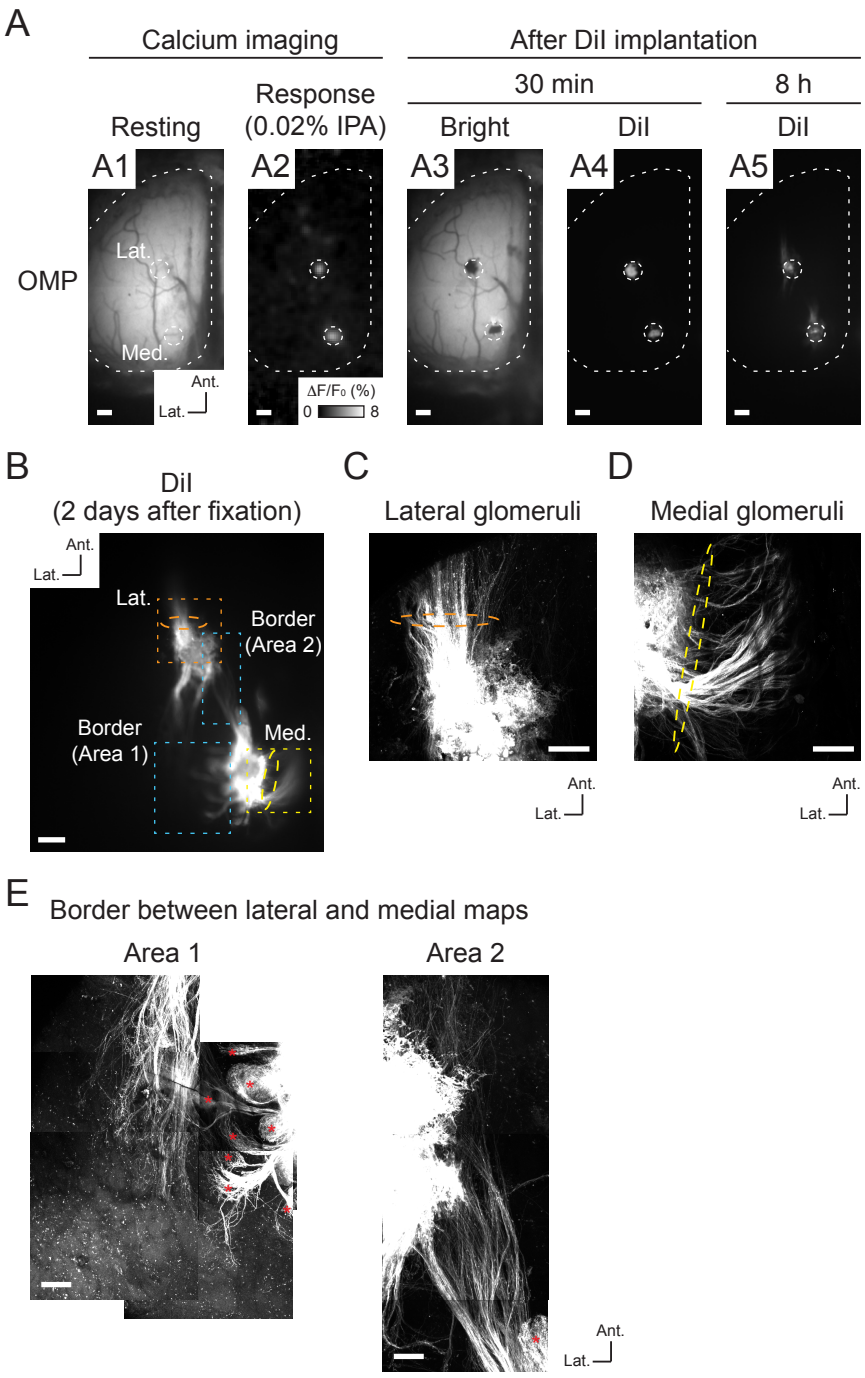

Figure 2: OSN axon trajectories for IPA-responsive glomeruli.
(A) Process for the DiI labeling of OSN axons. A1, resting fluorescence of GCaMP3 in the dorsal OB of OMP-Cre mouse; A2, IPA (0.02%)-responsive homologous glomeruli were observed by calcium imaging (color scale indicates ΔF/F0 [%] of GCaMP3 signal); A3, brightfield image after DiI implantation; A4, DiI fluorescence 30 min after DiI implantation; A5, DiI fluorescence 8 h after DiI implantation. The locations of IPA-responsive glomeruli are indicated by the white dotted circles. (B) Two-photon microscopy image of DiI-labeled glomeruli and OSN axons 2 days after DiI implantation. (C) Magnified image of area denoted by orange dotted square in B associated with lateral glomerulus. (D) Magnified image of area denoted by yellow dotted square in B associated with medial glomerulus. Two-photon microscopy images of OSN axons that transverse the lateral and medial surface of OB; orange and yellow dotted ellipses (in B, C, and D) represent major axonal projections from lateral and medial glomeruli. (E) Two-photon microscopy images of areas of lateral/medial border denoted by blue dotted square in B. Red asterisks indicate axon termination in several glomeruli in which the labeled OSNs probably passed through the surface of the DiI-implanted glomeruli. Some minor axons which did not show clear axon terminations in a glomerulus were observed in area 2 in this case. Ant., anterior. Lat., lateral. Scale bars, 200 μm in A and B, 50 μm in C and D, 100 μm in E.

expressing OSNs, respectively (Dewan et al., 2018, 2013; Pacifico et al., 2012; Zhang et al., 2013), we identified distinct pairs of glomeruli comprising OSNs and GABAergic, dopaminergic, and mitral/tufted cells in the caudal areas of the dorsal OB (Fig. 2A and Fig. 3A). The locations of these homologous glomeruli are consistent with the positions of glomeruli receiving inputs from TAAR3- and TAAR4-expressing neurons in previous reports (Dewan et al., 2018, 2013; Pacifico et al., 2012; Zhang et al., 2013).

To confirm that the glomeruli pairs represent medial and lateral maps, we retrogradely labeled TAAR3-expressing OSN axons by implanting the IPA-responsive glomeruli in OMP-GCaMP3 mice with DiI (1,1'-dioctadecyl-3,3,3'3'-tetramethylindocarbocyanine perchlorate) crystals. Optical observation performed 8 h later revealed labeling of OSN axons in both lateral and medial glomeruli (Fig. 2A5). These labeled axons were observed more clearly in fixed tissue 2 days later (Fig. 2B). Dorsolateral to the lateral IPA-responsive glomerulus, the majority of the labeled axons were oriented in an anterolateral direction (orange dashed ellipses in Fig. 2B and C). By contrast, the majority of axons dorsomedial to the medial IPA-responsive glomerulus were in an anteromedial direction (toward the septum) (yellow dotted ellipses in Fig. 2B and D). Notably, multiple glomerular structures were revealed by the terminal branches of labeled axons in the medial region (red asterisks in Fig. 2E), indicating that these axons originated from the medial side. Taken together, these results indicate that the pairs of recorded glomeruli were homologous pairs representing both lateral and medial maps. Therefore, our experimental design provides a unique opportunity to record simultaneously the odor-evoked neuronal activity of homologous glomeruli in the medial and lateral maps in OBs.

Similar temporal odor representations between medial and lateral maps in the OB.

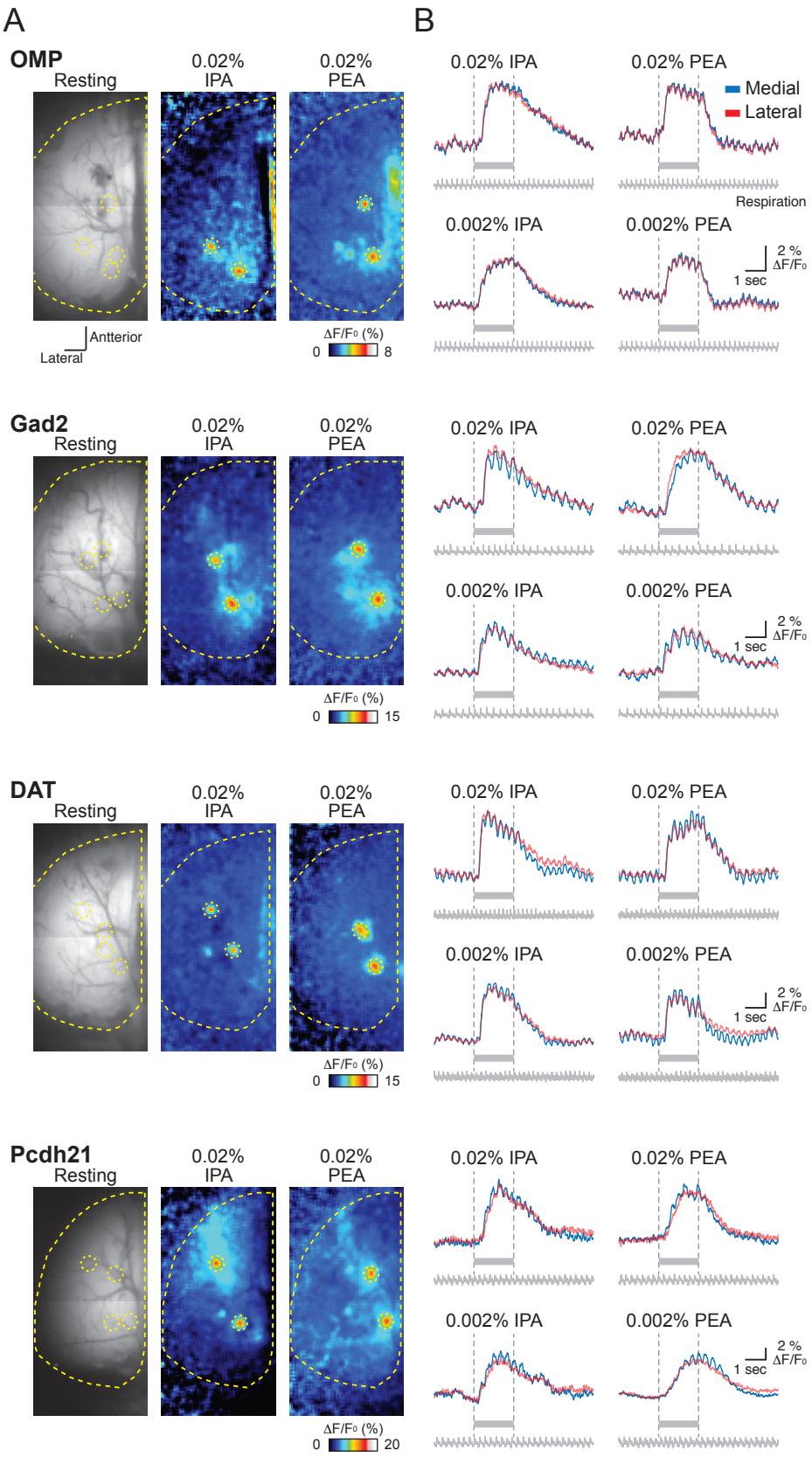

Figure 3: Odor-evoked response maps and traces among different types of OB neurons.
Odor-evoked response maps (A) and traces (B) from OMP-Cre, Gad2-Cre, DAT-Cre, and Pcdh21-Cre mice. Resting GCaMP3 fluorescence images are displayed in the left panels in A. Pseudocolored images in the middle and right panels in A indicate responses to 0.02% IPA and PEA, respectively. Yellow dotted lines and circles in each image show approximately the edge of the left OB and homologous glomeruli evoked by 0.02% IPA and PEA, respectively. The color scales represent ΔF/F0 (%) of GCaMP3 signal. Traces shown in B represent GCaMP3 fluorescence changes from two subsets of homologous glomeruli evoked by indicated concentrations of IPA and PEA shown in A. Red and blue traces indicate lateral and medial glomeruli, respectively. Gray bars under each trace and vertical dotted lines indicate the timing of odor stimulation. Respiration signals are also shown under the traces.

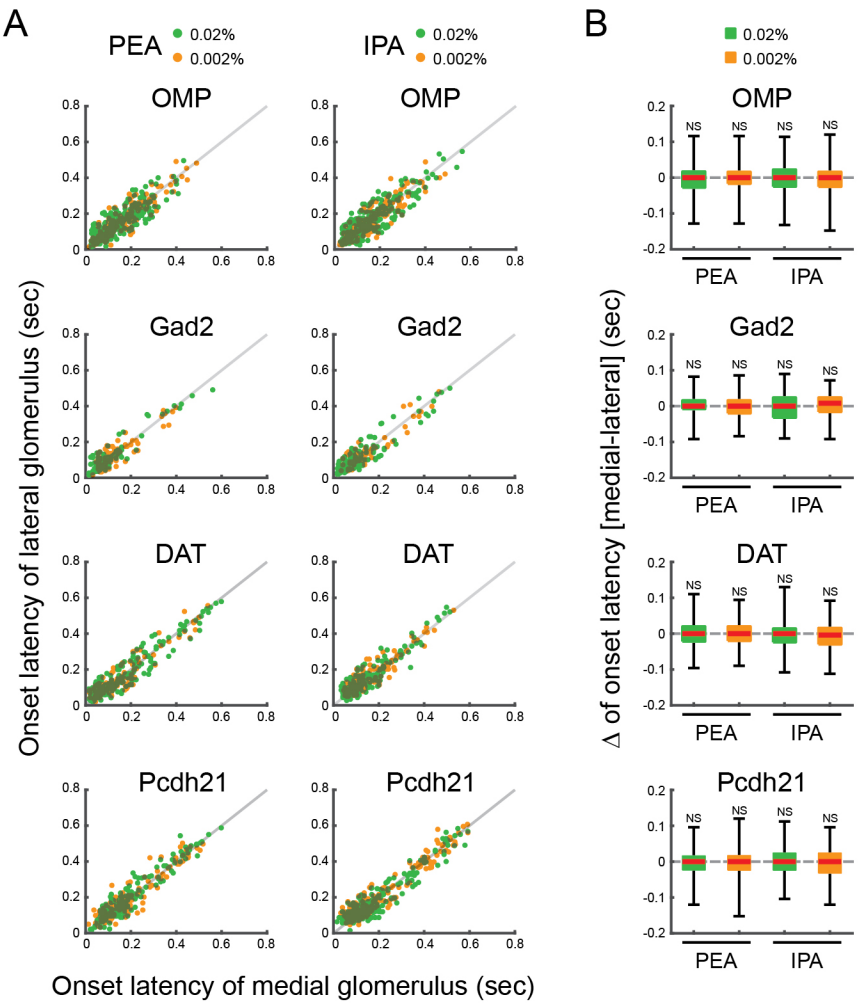

Figure 4: Onset latencies of medial and lateral glomeruli.
(A) Scatter plots displaying the distributions of onset latencies of medial and lateral glomeruli, which responded to PEA and IPA stimuli. x and y axes indicate onset latencies of medial and lateral glomerular responses, respectively. Individual green and orange dots indicate single trial data of 0.02% and 0.002% PEA or IPA. Gray lines indicate the equal onset latency time points of medial and lateral glomerular responses. (B) Box plots displaying the distributions of the differences of onset latencies between medial and lateral glomeruli responses to 0.02% and 0.002% PEA or IPA. Red horizontal lines in each box indicate the medians. Quartiles are shown as whiskers. NS, not significant (two-tailed paired Student's t test).

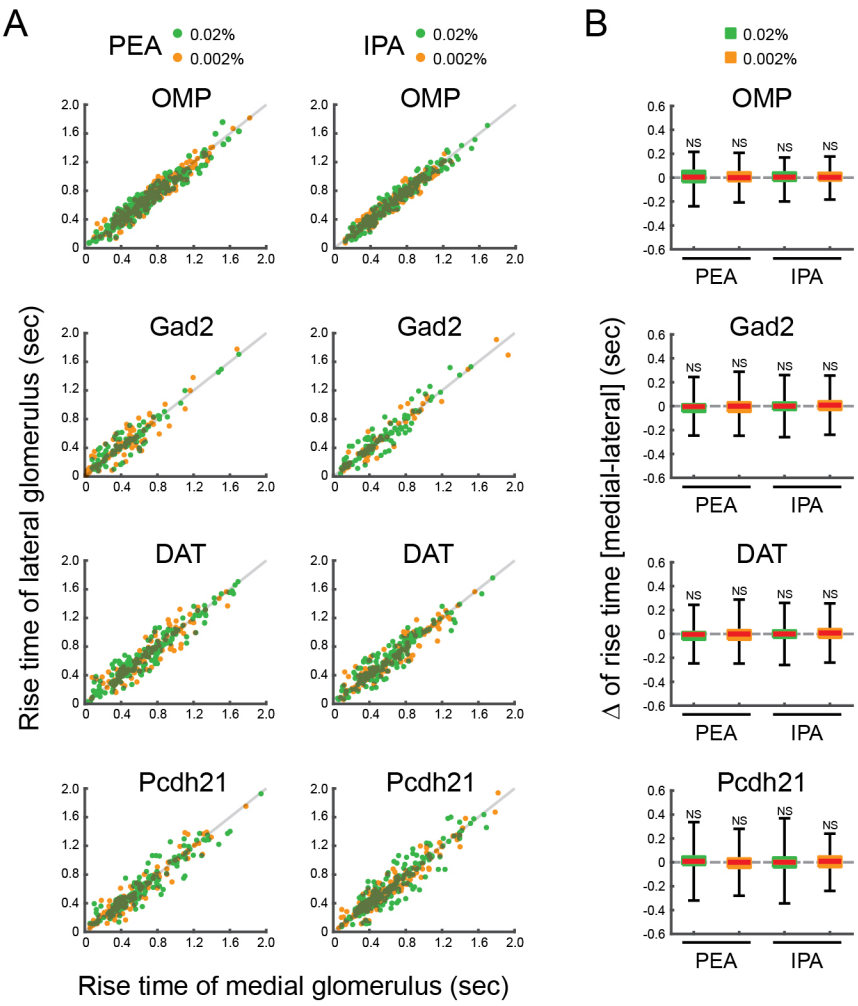

Figure 5: Rise times of medial and lateral glomeruli.
(A) Scatter plots displaying the distributions of rise times of the medial and lateral glomeruli, which responded to PEA and IPA stimuli. x and y axes indicate rise times of medial and lateral glomerular responses, respectively. Individual green and orange dots indicate single trial data of 0.02% and 0.002% PEA or IPA. Gray lines indicate the equal rise time points of medial and lateral glomerular responses. (B) Box plots displaying the distributions of the differences of rise times between medial and lateral glomerular responses to 0.02% and 0.002% PEA or IPA. Red horizontal lines in each box indicate the medians. Quartiles are shown as whiskers. NS, not significant (two-tailed paired Student's t test).

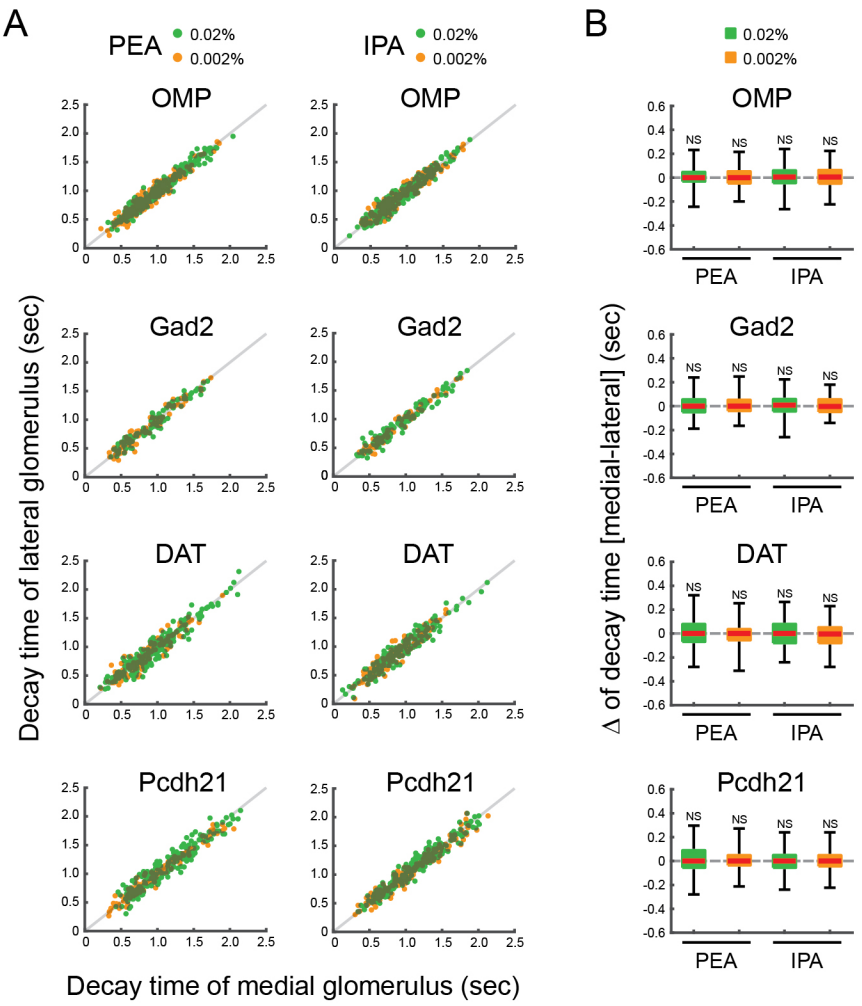

Figure 6: Decay times of medial and lateral glomeruli.
(A) Scatter plots displaying the distributions of decay times of the medial and lateral glomeruli, which responded to PEA and IPA stimuli. x and y axes indicate decay times of medial and lateral glomerular responses, respectively. Individual green and orange dots indicate single trial data of 0.02% and 0.002% PEA or IPA. Gray lines indicate the equal decay time points of medial and lateral glomerular responses. (B) Box plots displaying the distributions of the differences of decay times between medial and lateral glomerular responses to 0.02% and 0.002% PEA or IPA. Red horizontal lines in each box indicate the medians. Quartiles are shown as whiskers. NS, not significant (two-tailed paired Student's t test).

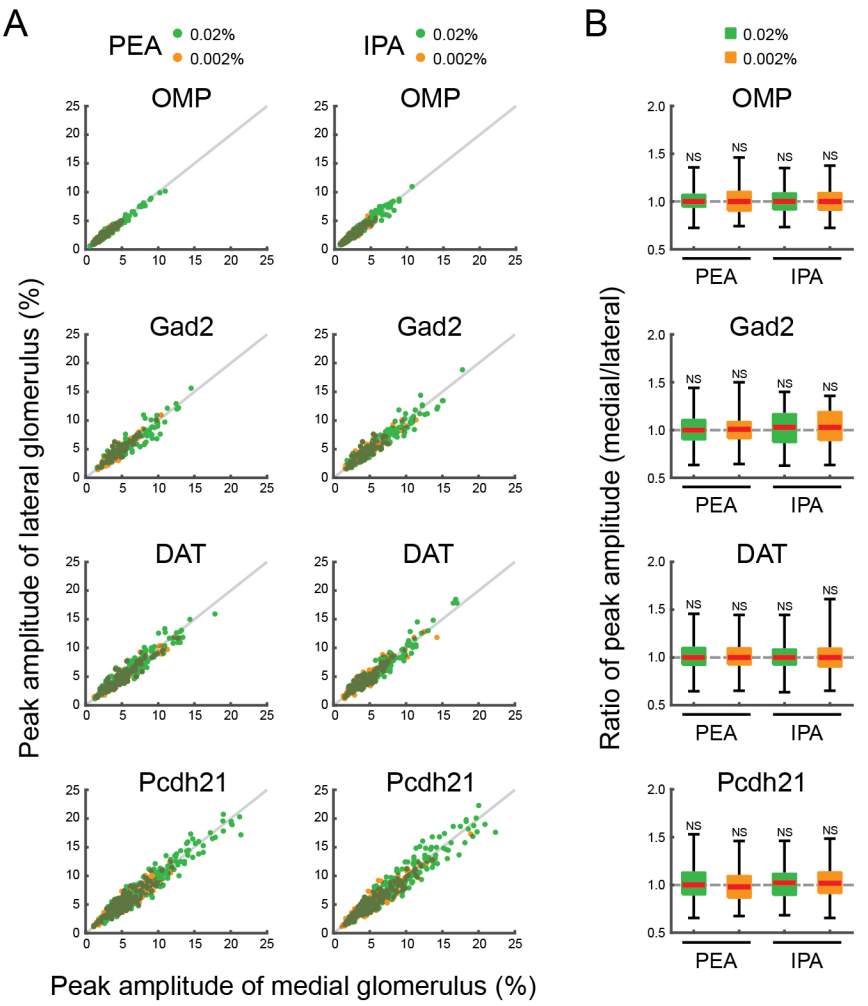

Figure 7: Peak amplitude of medial and lateral glomerular responses. (A) Scatter plots displaying the distributions of peak amplitudes of medial and lateral glomerular responses to PEA and IPA stimuli. x and y axes indicate peak amplitudes of medial and lateral glomerular responses, respectively. Individual green and orange dots indicate single trial data of 0.02% and 0.002% PEA or IPA. Gray lines indicate the equal peak amplitudes of medial and lateral glomerular responses. (B) Box plots displaying the distributions of the differences of peak amplitudes of medial and lateral glomerular responses to 0.02% and 0.002% PEA or IPA. Red horizontal lines in each box indicate the medians. Quartiles are shown as whiskers. NS, not significant (two-tailed paired Student's t test).

153 The medial and lateral glomeruli pairs represent inputs from odorant receptors of the same type
154 within medial and lateral regions, respectively, of the complex OE structure. Receptors in these
155 regions may be exposed to different air flow rates and mucosal volumes. We hypothesized that
156 these differences would be reflected in the timing of the glomeruli responses. However, the
157 calcium signals from all cell types examined in medial and lateral glomeruli in response to IPA
158 and PEA had similar amplitudes and temporal patterns (Fig. 3B). Further analyses revealed that
159 the timing of odor inputs to both maps was similar, as revealed by the onset latency measured as
160 the time at which the calcium signal exceeded the threshold from first inhalation during odor
161 stimulation (Fig. 4). The rise times of the responses, which are an indicator of response speed
162 and reflect the neuronal spike frequency, were similar between medial and lateral glomeruli (Fig.
163 5). The rise time was assessed as the duration for the calcium signal to increase from 20% to
164 80% of the peak signal. Conversely, the similar decay times, during which the calcium signal
165 decreased from 100% to 50% of the peak signals, suggested that the activity in one glomerulus
166 was not prolonged relative to the other after the odor stimulus was turned off (Fig. 6). Both
167 glomeruli in the pairs had responses that were similar in strength, as indicated by the peak
168 amplitudes (Fig. 7). Overall, there were no significant differences between paired glomeruli in
169 onset latency, rise time, decay time, and peak amplitude of the calcium responses in any of the
170 cell types studied (two-tailed paired *t* tests, see Table 1).
171
172 **Respiration-locked calcium fluctuations in medial maps are larger than in lateral maps.**
173 Oscillatory calcium responses associated with respiration were observed in the optical recordings
174 (Fig. 3B). These respiratory-linked fluctuations in calcium signals in medial glomeruli appeared
175 to be larger in the postsynaptic neurons (i.e., GABAergic, dopaminergic, and mitral/tufted cells

Figure 8

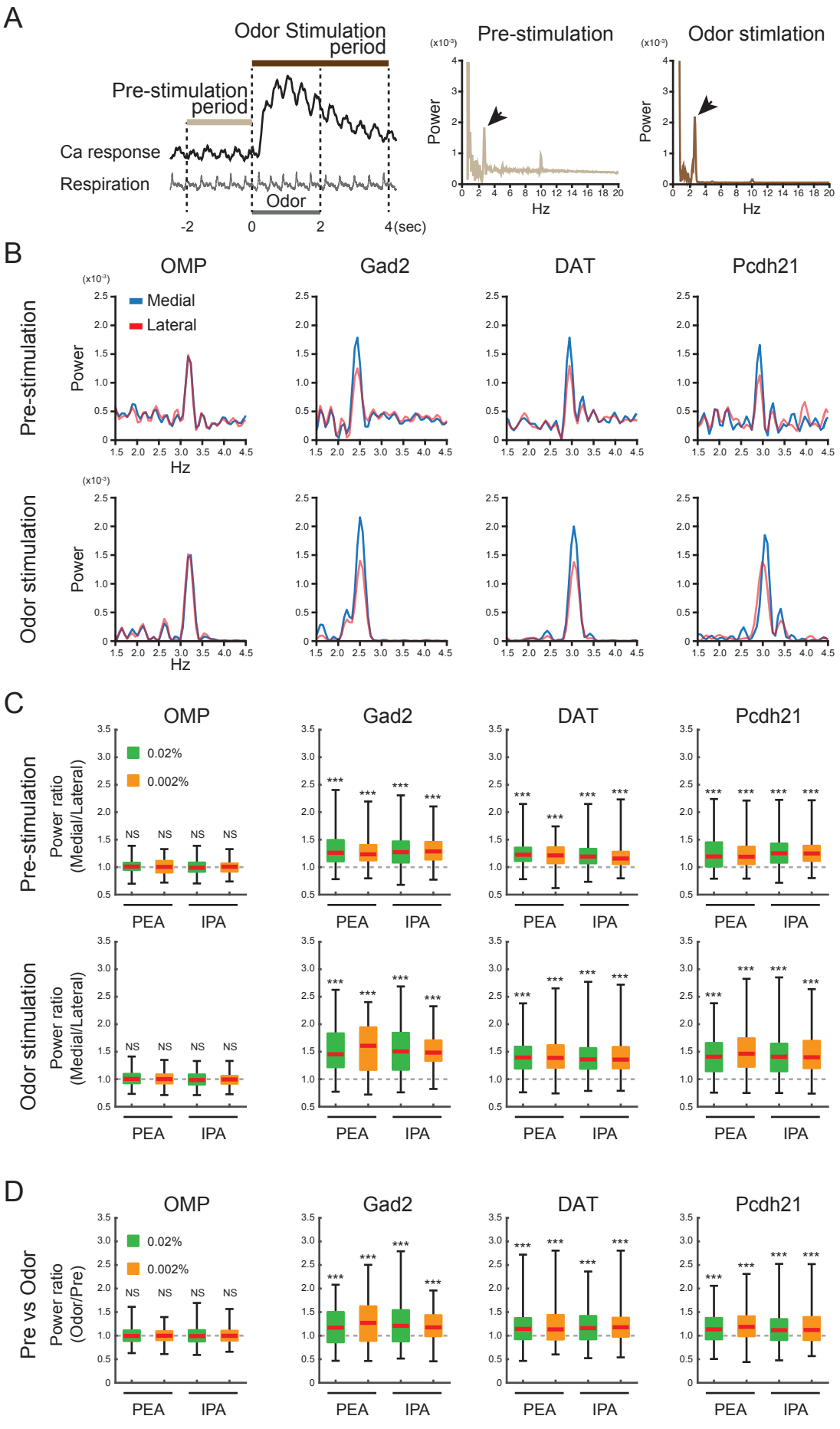

Figure 8: Respiration-locked calcium fluctuations of medial and lateral glomeruli.
(A) Schematic illustration of data collection time points and power spectral analysis. The prestimulation and odor stimulation periods are defined in left panel. Middle and right panels are representative examples of power spectral analyses with large frequency ranges in single trials. Respiration-locked fluctuations of calcium signals were prominently observed at 2–4 Hz (arrows). (B) Representative results of power spectral analyses of calcium signals during prestimulation (upper panels) and odor stimulation (lower panels) periods in neurons from GCaMP-expressing OMP-, Gad2-, DAT-, and Pcdh21-Cre mice. These calcium response traces are shown as 0.02% IPA response signals (as in Fig. 3B). Blue and red traces indicate medial and lateral glomeruli, respectively. (C) Comparisons of power spectra between the homologous glomeruli during the prestimulation (upper panels) and odor stimulation (lower panels) period in neurons from OMP-, Gad2-, DAT-, and Pcdh21-Cre mice. The ratios of peak powers were calculated by dividing the medial glomerular power by the lateral glomerular power in each trial. (D) Comparisons of peak power between the prestimulation and odor stimulation periods. The power ratios were calculated by dividing the odor stimulation period power (lower panels in C) by the prestimulation-period power (show in C, upper panels). Red horizontal lines in each box show medians. Quartiles are shown as whiskers. NS, not significant; ***; $p < 0.001$ two-tailed paired Student's t test).

176 in the Gad2-Cre, DAT-Cre, and Pcdh21-Cre lines, respectively) than in the OSNs (i.e., cells in
177 the OMP-Cre line). To examine this quantitatively, we applied a power spectral analysis to the
178 data. Power spectra before and during odor stimulation displayed peak frequencies of 2–4 Hz
179 (arrows in Fig. 8A), which matches the respiration rhythm under our experimental conditions.
180 These respiration-locked calcium oscillations were detected in all the cell types (Fig. 8B). The
181 peak power spectra at 2–4 Hz were indeed larger in medial glomeruli than in lateral glomeruli
182 from Gad2-, DAT-, and Pcdh21-Cre mice both before and after odor stimulation but not in
183 OMP-Cre mice. The statistical analysis is summarized in Fig. 8C (two-tailed paired *t* tests, see
184 Table 1; the datasets are the same as in Fig. 4–7). In addition, the medial/lateral power ratios for
185 spectra from postsynaptic neurons were larger during odor stimulation than before stimulation
186 (Fig. 8D), suggesting a strong influence of the odor stimulus on the size of the fluctuation. These
187 differences were observed consistently with 0.02% and 0.002% PEA and IPA (two-tailed paired
188 *t* tests, see Table 1). These results suggest that respiration-locked calcium fluctuations in the
189 medial maps are enhanced postsynaptically in the OB by odorant stimulation.

Table 1

Figure	Mice	Odorant	Conc.	*p* value
4B	OMP	PEA	0.02%	0.1296
4B	OMP	PEA	0.002%	0.8526
4B	OMP	IPA	0.02%	0.1721
4B	OMP	IPA	0.002%	0.3464
4B	Gad2	PEA	0.02%	0.1014
4B	Gad2	PEA	0.002%	0.5423
4B	Gad2	IPA	0.02%	0.8620
4B	Gad2	IPA	0.002%	0.5818
4B	DAT	PEA	0.02%	0.9053
4B	DAT	PEA	0.002%	0.9828
4B	DAT	IPA	0.02%	0.1108
4B	DAT	IPA	0.002%	0.0804
4B	Pcdh21	PEA	0.02%	0.4278
4B	Pcdh21	PEA	0.002%	0.1816
4B	Pcdh21	IPA	0.02%	0.6100
4B	Pcdh21	IPA	0.002%	0.1658
5B	OMP	PEA	0.02%	0.1331
5B	OMP	PEA	0.002%	0.1783
5B	OMP	IPA	0.02%	0.2068
5B	OMP	IPA	0.002%	0.2453
5B	Gad2	PEA	0.02%	0.0977
5B	Gad2	PEA	0.002%	0.9225
5B	Gad2	IPA	0.02%	0.2570
5B	Gad2	IPA	0.002%	0.5774
5B	DAT	PEA	0.02%	0.5551
5B	DAT	PEA	0.002%	0.8928
5B	DAT	IPA	0.02%	0.1158
5B	DAT	IPA	0.002%	0.5407
5B	Pcdh21	PEA	0.02%	0.1650
5B	Pcdh21	PEA	0.002%	0.7446
5B	Pcdh21	IPA	0.02%	0.5037
5B	Pcdh21	IPA	0.002%	0.2666
6B	OMP	PEA	0.02%	0.4187
6B	OMP	PEA	0.002%	0.5834
6B	OMP	IPA	0.02%	0.2886
6B	OMP	IPA	0.002%	0.5170
6B	Gad2	PEA	0.02%	0.7568
6B	Gad2	PEA	0.002%	0.8668
6B	Gad2	IPA	0.02%	0.2757
6B	Gad2	IPA	0.002%	0.8687
6B	DAT	PEA	0.02%	0.4066
6B	DAT	PEA	0.002%	0.7572
6B	DAT	IPA	0.02%	0.7893
6B	DAT	IPA	0.002%	0.2148
6B	Pcdh21	PEA	0.02%	0.6586
6B	Pcdh21	PEA	0.002%	0.3455
6B	Pcdh21	IPA	0.02%	0.3366
6B	Pcdh21	IPA	0.002%	0.1663
7B	OMP	PEA	0.02%	0.3851
7B	OMP	PEA	0.002%	0.8639
7B	OMP	IPA	0.02%	0.2743
7B	OMP	IPA	0.002%	0.7079
7B	Gad2	PEA	0.02%	0.6291
7B	Gad2	PEA	0.002%	0.5314
7B	Gad2	IPA	0.02%	0.0769
7B	Gad2	IPA	0.002%	0.4791
7B	DAT	PEA	0.02%	0.6461
7B	DAT	PEA	0.002%	0.4716
7B	DAT	IPA	0.02%	0.6236
7B	DAT	IPA	0.002%	0.6799
7B	Pcdh21	PEA	0.02%	0.6480
7B	Pcdh21	PEA	0.002%	0.2161
7B	Pcdh21	IPA	0.02%	0.6518
7B	Pcdh21	IPA	0.002%	0.1591
8C Pre	OMP	PEA	0.02%	0.2291
8C Pre	OMP	PEA	0.002%	0.7955
8C Pre	OMP	IPA	0.02%	0.4799
8C Pre	OMP	IPA	0.002%	0.5202
8C Pre	Gad2	PEA	0.02%	1.337E-09
8C Pre	Gad2	PEA	0.002%	2.453E-13
8C Pre	Gad2	IPA	0.02%	8.218E-08
8C Pre	Gad2	IPA	0.002%	4.121E-11
8C Pre	DAT	PEA	0.02%	2.031E-29
8C Pre	DAT	PEA	0.002%	1.344E-11
8C Pre	DAT	IPA	0.02%	3.134E-24
8C Pre	DAT	IPA	0.002%	2.399E-13
8C Pre	Pcdh21	PEA	0.02%	8.012E-09
8C Pre	Pcdh21	PEA	0.002%	6.231E-11
8C Pre	Pcdh21	IPA	0.02%	8.138E-18
8C Pre	Pcdh21	IPA	0.002%	1.721E-18
8C Odor	OMP	PEA	0.02%	0.8207
8C Odor	OMP	PEA	0.002%	0.4752
8C Odor	OMP	IPA	0.02%	0.1282
8C Odor	OMP	IPA	0.002%	0.1916
8C Odor	Gad2	PEA	0.02%	1.343E-09
8C Odor	Gad2	PEA	0.002%	7.850E-10
8C Odor	Gad2	IPA	0.02%	7.617E-16
8C Odor	Gad2	IPA	0.002%	1.781E-11
8C Odor	DAT	PEA	0.02%	9.577E-18
8C Odor	DAT	PEA	0.002%	1.405E-10
8C Odor	DAT	IPA	0.02%	1.279E-19
8C Odor	DAT	IPA	0.002%	2.311E-08
8C Odor	Pcdh21	PEA	0.02%	1.734E-15
8C Odor	Pcdh21	PEA	0.002%	2.535E-09
8C Odor	Pcdh21	IPA	0.02%	4.144E-18
8C Odor	Pcdh21	IPA	0.002%	1.778E-14
8D	OMP	PEA	0.02%	0.7834
8D	OMP	PEA	0.002%	0.6397
8D	OMP	IPA	0.02%	0.5733
8D	OMP	IPA	0.002%	0.5445
8D	Gad2	PEA	0.02%	4.175E-05
8D	Gad2	PEA	0.002%	1.267E-05
8D	Gad2	IPA	0.02%	7.056E-07
8D	Gad2	IPA	0.002%	6.139E-04
8D	DAT	PEA	0.02%	2.906E-08
8D	DAT	PEA	0.002%	9.435E-08
8D	DAT	IPA	0.02%	5.601E-11
8D	DAT	IPA	0.002%	1.080E-07
8D	Pcdh21	PEA	0.02%	1.570E-08
8D	Pcdh21	PEA	0.002%	7.645E-10
8D	Pcdh21	IPA	0.02%	2.666E-09
8D	Pcdh21	IPA	0.002%	2.909E-09

Discussion

Pre/postsynaptic calcium events in multiple cell types.

In this work, GCaMP was expressed in postsynaptic GABAergic, dopaminergic, and mitral/tufted cells and in presynaptic axon terminals of OSNs of mice from various transgenic Cre-driver lines. Calcium signaling in OSNs reflects activation resulting in transmitter release, whereas calcium signaling in the other cell types may reflect activation of calcium-permeable glutamate receptors and the opening of calcium channels in response to excitatory postsynaptic potentials or spikes initiated in the dendrites or soma (Burnashev et al., 1992; Chen et al., 1997; Halabisky et al., 2000; Helmchen et al., 1999; Nagayama et al., 2007; Svoboda et al., 1999). Therefore, the calcium influxes in these cells are controlled by different biophysical mechanisms and represent different aspects of biological events. These differences would not impact our imaging results, as the comparisons were between medial and lateral glomeruli comprising the same cell types. Notably, we did not observe cell-type-specific differences between the medial and lateral maps at the glomerular level, which is consistent with recent data at the single-cell level showing that odorant responses of juxtaglomerular cells are associated with the same glomerulus putatively (Homma et al., 2019). Nevertheless, we cannot exclude the possibility of differential response timing by different cell types, because the time resolution for calcium imaging was limited and did not reflect that activity of all neurons within a glomerulus. Future studies may begin to address this by imaging spike activity at a single-cell resolution.

Response timing of the homologous glomeruli in medial and lateral maps.

A pioneer electrophysiological study using a unique transgenic mouse line in which all OSNs express the same odorant receptor suggested that that the latencies of mitral cell responses to

odorant stimulation are shorter in the medial map than in the lateral map, especially at a low odorant concentration (Zhou and Belluscio, 2012). Because the OE is a complicated structure, airflow speed likely varies throughout the nasal cavity, and odorants may reach different areas at different times (Kimbell et al., 1997; Schoenfeld and Cleland, 2006; Zhao et al., 2006). This would produce a time lag for odorant responses in medial and lateral neurons. However, we did not observe different onset latencies between homologous medial and lateral glomeruli, even at low odorant concentrations. This may be because our recordings were via optical imaging rather than electrophysiology and from glomerular rather than MCLs. Another possible reason is the difference in OB regions recorded, which reflect inputs from different OE regions. Our study was restricted to a small region of the posteromedial dorsal OB, which receives inputs from the dorsal OE (Miyamichi et al., 2005). The dorsal OE faces the large nasal cavity and has a relatively simple wall structure compared with that of ventral zones. Moreover, OSNs projecting to medial and lateral maps are close together in the dorsal OE, for which any latency would not be detectable under our experimental conditions. It is possible that differential latencies from neurons in the ventral OB may be larger or more easily detected (Kimbell et al., 1997; Schoenfeld and Cleland, 2006; Zhao et al., 2006). In other words, the time lag may gradually become larger along the dorsal-ventral axis in the OB.

Neuronal/circuitry mechanism of respiration-locked calcium fluctuations

The fluctuations of calcium responses, which corresponded to the rhythm of respiration, were larger in medial glomeruli than in lateral glomeruli. This may reflect differential airflow volumes or rates along the medial and lateral sides of the nostril. As this was only observed in postsynaptic calcium responses, the modulation is likely not within the OE but in the OB. The

mechanism for this modulation may involve the physiological properties of these and/or associated neurons in medial and lateral glomeruli, such as differences in the expression of various calcium and/or other essential channels. As we did not observe differences in the amplitudes of the calcium responses, more than one channel type may be involved. Differential expression of other essential molecules would also change neuronal and/or network excitability. Neurons in medial glomeruli may also increase and decrease their intracellular calcium levels more synchronously during inhalation and exhalation, respectively. Such synchrony would be expected to affect the overall activity of neurons within a glomerulus; this could more directly be addressed by studies recording neuronal spikes in the context of a circuit. Thus, further investigations are needed to determine the mechanism by which calcium fluctuations are larger in medial glomeruli than in lateral glomeruli in response to odorant stimulation.

Inhibitory connections between the two maps

Tufted cells in the lateral glomeruli project to cells in the internal plexiform and superficial GCLs underlying the medial glomeruli receiving inputs from the same odorant receptors, and vice versa. These projections activate granule cells and thus inhibit surrounding mitral/tufted cells (Belluscio and Katz, 2001; Lodovichi et al., 2003; Zhou and Belluscio, 2008), resulting in mutual inhibition between the medial and lateral maps. Our data suggest this inhibition is not simple (i.e., one glomerulus is inhibited when the other is activated), as medial and lateral glomeruli are activated simultaneously during odor stimulation. The similar temporal patterns and the absence of counterphase-locked activity between the two glomeruli also suggest that the activity of one glomerulus does not inhibit the other homologous glomerulus in a given time phase, such as during inhalation or exhalation. The functional role of these mutual inhibitory

connections and how they contribute to odor processing remain unknown. It is possible that these connections regulate the temporal activity pattern and/or synchrony of neurons or glomeruli in both maps.

Odor information processing streams from the medial and lateral maps

One of the unresolved issues is where the medial and lateral maps project and how higher brain centers handle these two outputs. Current knowledge of the connections between the OB and the olfactory cortex (Ghosh et al., 2011; Igarashi et al., 2012; Miyamichi et al., 2011; Nagayama et al., 2010; Sosulski et al., 2011) suggest that there may not be dramatic differences regarding where the maps project. However, it is still not known whether the outputs from the two maps are evenly transmitted to all olfactory cortical areas, and some regions may preferentially receive input from one or the other. More detailed knowledge of the cortical projections may help reveal the significance of the multiple maps and how the information from the two information streams is compiled in higher brain centers.

Rhythm of respiration

In vertebrate land animals, airflow through the nasal cavity during respiration alternates between orthonasal and retronasal directions. This induces a synchronized rhythm in the olfactory system, which contributes to the odor information process (Cury and Uchida, 2010; Spors and Grinvald, 2002; Uchida et al., 2014; Wilson and Mainen, 2006). Moreover, the orthonasal and retronasal airflows switch the perception from smells originating from the surrounding environment to taste in the mouth, respectively (Gautam and Verhagen, 2012; Shepherd, 2012). In addition to olfactory areas, respiration-locked oscillations have been observed in hippocampus as well as

barrel and prefrontal cortices in the rodent (Biskamp et al., 2017; Lockmann et al., 2016; Nguyen Chi et al., 2016; Phillips et al., 2012; Shusterman et al., 2011; Yanovsky et al., 2014). In the barrel cortex, phase-locked oscillation patterns coordinate the interaction between olfaction and tactile sensations (Ito et al., 2014), whereas freezing behavior is modulated by rhythmic activity in prelimbic prefrontal cortex driven by inputs from the anterior olfactory nucleus (Moberly et al., 2018), which has topographical connections to the OB (Schoenfeld et al., 1985; Yan et al., 2008). The anterior olfactory nucleus sub-region which dominantly primarily receive inputs from the medial map may relay this information to higher brain centers controlling respiration-linked neuronal activity associated with mouse behavior. Thus, the anterior olfactory nucleus may be responsible for processing information from multiple glomerular maps and represents an area that warrants further study.

Materials and Methods

All procedures were performed on mice of either sex in accordance with National Institutes of Health guidelines and approved by the Animal Welfare Committee at the University of Texas Health Science Center at Houston.

Animals.

Cre-inducible GCaMP3-expressing mice (Ai38; #014538, Jackson Laboratory, Bar Harbor, ME) (Zariwala et al., 2012) were used for the expression of the calcium indicator in target neurons. This mouse line was crossed with the following Cre-driver mouse lines: OMP-Cre (for OSNs, #006668; Jackson Laboratory) (Li et al., 2004), Gad2-Cre (for GABAergic neurons, #010802; Jackson Laboratory) (Taniguchi et al., 2011), DAT-Cre (for dopaminergic neurons, #006660; Jackson Laboratory) (Bäckman et al., 2006), and Pcdh21-Cre (for mitral/tufted cells, #02189; RIKEN BioResource Research Center, Tsukuba, Japan) (Nagai et al., 2005).

Histology.

Mice were deeply anesthetized and fixed by transcardial perfusion with 4% paraformaldehyde (PFA) in 0.1 M phosphate buffer (PB; pH 7.4). Then, whole brains were dissected out and postfixed in 4% PFA/0.1 M PB overnight. The samples were cryoprotected in 30% sucrose (wt/vol) in phosphate-buffered saline (PBS; pH 7.4) and embedded in optimal cutting temperature compound (Fisher HealthCare, Waltham, MA). Olfactory tissue sections 30-μm thick were cut on a cryostat, washed with PBS, and mounted with Fluoroshield mounting medium (F6057; Sigma-Aldrich, St. Louis, MO). Images were captured on an Olympus FluoView FV1000 laser scanning confocal microscope using a 20×/0.75 NA lens objective

(UPLSAPO 20X; Olympus, Tokyo, Japan).

Odorant stimulation.

IPA (#126810; Sigma-Aldrich) and PEA (#128945; Sigma-Aldrich) were diluted in mineral oil (M3516; Sigma-Aldrich) to 0.1% and 0.01% in glass vials. The odorants were vaporized using nitrogen, mixed with filtered air to final concentrations of 0.02% and 0.002% with 0.5 liter/min air flow rate, and then delivered to mouse nostrils using a custom-made olfactometer (Kikuta et al., 2013). The odorants were presented for 2 s with an interstimulus interval of >60 s to avoid sensory adaptation.

***In vivo* optical imaging.**

GCaMP-expressing mice were anesthetized with urethane (1.2 g/kg of body weight, intraperitoneal). The depth of anesthesia was monitored by toe pinches throughout the experiment. Body temperature was kept between 36.0°C and 37.0°C with a heating pad. The skull over the OBs was carefully thinned with a dental drill and covered with 1.2% agarose dissolved in saline and with a 4–6-mm^2 coverslip (thickness, #1). Odor-evoked GCaMP3 signals were recorded through a 5× lens objective (Fluar 5×/0.25; Zeiss, Oberkochen, Germany) on a microscope (SliceScope; Scientifica, Uckfield, United Kingdom) equipped with a high-speed charge-coupled-device camera (NeuroCCD-SM256; RedShirtImaging, Decatur, GA) at 125 Hz (128 × 128 pixels) for 12 s, which included a 4-s prestimulus period and a 2-s odor presentation period. Excitation light was provided using a 470-nm light-emitting diode module (M470L2; Thorlabs, Newton, NJ). A standard green fluorescent protein filter set (BrightLine GFP-4050A-OMF-ZERO; Semrock, Rochester, NY) was used to detect the GCaMP3 signal. Chest movement

of the animals was monitored to measure the respiratory rhythm during the optical imaging period.

DiI labeling of OSN axons.

After calcium imaging, the skull over the dorsal OBs was removed. Then, small DiI crystals were attached to the tip of glass capillaries (tip diameter, ~5 μm) and embedded into the area of IPA-responsive glomeruli. The positions of blood vessels relative to identical pairs of glomeruli were used as landmarks for DiI implantation. The mice remained anesthetized for 9–10 h after DiI implantation and then were fixed by transcardial perfusion with 4% PFA/0.1 M PB. Whole brains were removed and incubated in PBS at room temperature until observation. Low-magnification images were captured by a charge-coupled-device camera (NeuroCCD-SM256 or SensiCam; PCO, Kelheim,Germany) using a 5× lens objective (Fluar 5×/0.25, Zeiss) with a light-emitting diode module (MCWHL2-C1; Thorlabs) and a standard Cy3 cube (BrightLine Cy3-4040C-OMF-ZERO; Semrock). For high-magnification views of OSN axons, images were acquired with a two-photon microscope (Prairie Ultima; Bruker, Billerica, MA), using a 20× water immersion lens objective (UMPLFLH 20XW; Olympus), with a 5-μm inter-z-slice interval and 512 × 512 pixel resolution. DiI was excited at 920 nm (Ti:sapphire laser, MaiTai HP DS; Spectra-Physics, Santa Clara, CA), and DiI fluorescence was detected with an emission filter cube (575-nm dichroic mirror and 607/45-nm barrier filters).

Data analysis for wide-field calcium imaging data.

Odor-evoked response maps were generated using Fiji/ImageJ (Schindelin et al., 2012) with custom-written scripts. Spatially filtered (3 × 3 mean filter) prestimulation-period images (4 s)

were averaged and used as a baseline (F_0). Images averaged 3 s after the onset of the 1-s odor stimulation were used as the response image (F). Then, F was subtracted from F_0 to obtain the difference (ΔF). ΔF values were divided by F_0 to obtain the ratio image ($\Delta F/F_0$). Spatial filters (3 × 3 mean filter) were also applied to the ratio images. All negative values were set to zero in the images. Regions of interest corresponding to glomeruli were manually set (4–8 pixels centered on each glomeruli).

The time courses of calcium signals (see Fig. 3B) were calculated using MATLAB (MathWorks, Natick, MA) with custom-written scripts. $\Delta F/F_0$ values were calculated using the same procedure described above but with a temporal filter (3 frames average, 24 ms) rather than a spatial filter applied to the $\Delta F/F_0$ values.

Onset latency, rise time, decay time, and peak amplitude were computed with custom MATLAB scripts. First, the baseline values ($\Delta F/F_0$) were determined as the mean values over the baseline period, which were defined as the 80-ms time window immediately before stimulation onset. Then, the noise level in each trial was defined as the minimum standard deviation among eight 0.5-s blocks in the 4-s prestimulation period. The onset latency was determined as the first time point at which all data points in the subsequent 80 ms exceeded the threshold (2.5 times the noise level). The onset latency was measured as the time elapsed from the first inhalation after the onset of odor presentation. The rise time was defined as the duration the calcium signals increased from 20% to 80% of peak amplitude. Time points for when the calcium signals reached 20% and 80% of the peak amplitude were set as the earliest time point after which half of the data points in the subsequent 80 ms exceeded these criteria. The decay time was defined as the duration the calcium signal decreased from 100% to 50% of the peak amplitude. Time points for when the calcium signals reached 100% and 50% of peak amplitude were set as the earliest

time point after which half of data points in the subsequent 80 ms dropped below these criteria. The peak amplitude was measured as the maximum value using the 80-ms time window moving average, which reflects average of 9 sequential data points, after stimulation onset.

To analyze fluctuations in the calcium fluorescence, a power spectral analysis based on Fourier transform was used. First, $\Delta F/F_0$ values were preprocessed with a 40-ms box filter and divided into two periods, corresponding to prestimulation (2 s before onset of odor stimulation) and odor stimulation (4 s after onset of odor stimulation). Then, a power spectrum was computed by using Fast Fourier transform with 2,048 points (using a built-in function of MATLAB [fft.m]) in each period. Because we used a 125-Hz sampling frequency, the frequency resolution is 0.061 Hz. The peak power in each period was determined as the maximum value between 2 and 4 Hz.

Statistics.

Statistical analyses were performed using Microsoft Excel 2013. All statistical significance was determined by a two-tailed paired Student's *t* test; *p* values of <0.05 were considered statistically significant. Data are presented as scatter and box-whisker plots of pooled data sets for a given odorant and concentration from OMP- (279 trials in 0.02% PEA, 194 trials in 0.002% PEA, 297 trials in 0.02% IPA, and 185 trials in 0.002% IPA; $n = 10$), Gad2- (106 trials in 0.02% PEA, 84 trials in 0.002% PEA, 119 trials in 0.02% IPA, and 62 trials in 0.002% IPA; $n = 6$), DAT- (216 trials in 0.02% PEA, 118 trials in 0.002% PEA, 184 trials in 0.02% IPA, and 123 trials in 0.002% IPA; $n = 6$), and Pcdh21-Cre (199 trials in 0.02% PEA, 130 trials in 0.002% PEA, 241 trials in 0.02% IPA, and 176 trials in 0.002% IPA; $n = 6$) mice. In scatter plots, individual dots show data points from single trials. In box-whisker plots, horizontal red lines and boxes indicate the medians and quartiles, respectively. The whiskers go from each quartile to the minimum or

maximum. All *p* values calculated in this study are listed in Table 1.

Acknowledgements

We thank Dr. Dewan for discussions of odorant response properties and the location of TAAR glomeruli.

Competing interests

None.

References

Bäckman CM, Malik N, Zhang Y, Shan L, Grinberg A, Hoffer BJ, Westphal H, Tomac AC. 2006. Characterization of a mouse strain expressing Cre recombinase from the 3′ untranslated region of the dopamine transporter locus. *genesis* **44**:383–390. doi:10.1002/dvg.20228

Belluscio L, Katz LC. 2001. Symmetry, stereotypy, and topography of odorant representations in mouse olfactory bulbs. *J Neurosci* **21**:2113–22.

Belluscio L, Lodovichi C, Feinstein P, Mombaerts P, Katz LC. 2002. Odorant receptors instruct functional circuitry in the mouse olfactory bulb. *Nature* **419**:296–300. doi:10.1038/nature01001

Biskamp J, Bartos M, Sauer J-F. 2017. Organization of prefrontal network activity by respiration-related oscillations. *Sci Rep* **7**:45508. doi:10.1038/srep45508

Buck LB. 1996. Information Coding in the Vertebrate Olfactory System. *Annu Rev Neurosci* **19**:517–544. doi:10.1146/annurev.ne.19.030196.002505

Burnashev N, Khodorova A, Jonas P, Helm PJ, Wisden W, Monyer H, Seeburg PH, Sakmann B. 1992. Calcium-permeable AMPA-kainate receptors in fusiform cerebellar glial cells. *Science* **256**:1566–70.

Chen WR, Midtgaard J, Shepherd GM. 1997. Forward and backward propagation of dendritic impulses and their synaptic control in mitral cells. *Science* **278**:463–7.

Cury KM, Uchida N. 2010. Robust odor coding via inhalation-coupled transient activity in the mammalian olfactory bulb. *Neuron* **68**:570–85. doi:10.1016/j.neuron.2010.09.040

Dewan A, Cichy A, Zhang J, Miguel K, Feinstein P, Rinberg D, Bozza T. 2018. Single olfactory receptors set odor detection thresholds. *Nat Commun* **9**:2887. doi:10.1038/s41467-018-

05129-0

Dewan A, Pacifico R, Zhan R, Rinberg D, Bozza T. 2013. Non-redundant coding of aversive odours in the main olfactory pathway. *Nature* **497**:486–489. doi:10.1038/nature12114

Ferrero DM, Lemon JK, Fluegge D, Pashkovski SL, Korzan WJ, Datta SR, Spehr M, Fendt M, Liberles SD. 2011. Detection and avoidance of a carnivore odor by prey. *Proc Natl Acad Sci* **108**:11235–11240. doi:10.1073/pnas.1103317108

Gautam SH, Verhagen J V. 2012. Retronasal Odor Representations in the Dorsal Olfactory Bulb of Rats. *J Neurosci* **32**:7949–7959. doi:10.1523/JNEUROSCI.1413-12.2012

Ghosh S, Larson SD, Hefzi H, Marnoy Z, Cutforth T, Dokka K, Baldwin KK. 2011. Sensory maps in the olfactory cortex defined by long-range viral tracing of single neurons. *Nature* **472**:217–220. doi:10.1038/nature09945

Halabisky B, Friedman D, Radojicic M, Strowbridge BW. 2000. Calcium influx through NMDA receptors directly evokes GABA release in olfactory bulb granule cells. *J Neurosci* **20**:5124–34.

Helmchen F, Svoboda K, Denk W, Tank DW. 1999. In vivo dendritic calcium dynamics in deep-layer cortical pyramidal neurons. *Nat Neurosci* **2**:989–996. doi:10.1038/14788

Homma R, Lv X, Sato T, Imamura F, Zeng S, Nagayama S. 2019. Narrowly Confined and Glomerulus-Specific Onset Latencies of Odor-Evoked Calcium Transients in the Juxtaglomerular Cells of the Mouse Main Olfactory Bulb. *eneuro* **6**:ENEURO.0387-18.2019. doi:10.1523/ENEURO.0387-18.2019

Huang L, Garcia I, Jen H-I, Arenkiel BR. 2013. Reciprocal connectivity between mitral cells and external plexiform layer interneurons in the mouse olfactory bulb. *Front Neural Circuits* **7**:32. doi:10.3389/fncir.2013.00032

462 Igarashi KM, Ieki N, An M, Yamaguchi Y, Nagayama S, Kobayakawa K, Kobayakawa R,
463 Tanifuji M, Sakano H, Chen WR, Mori K. 2012. Parallel mitral and tufted cell pathways
464 route distinct odor information to different targets in the olfactory cortex. *J Neurosci*
465 **32**:7970–85. doi:10.1523/JNEUROSCI.0154-12.2012
466 Inaki K, Takahashi YKYK, Nagayama S, Mori K. 2002. Molecular-feature domains with
467 posterodorsal-anteroventral polarity in the symmetrical sensory maps of the mouse olfactory
468 bulb: Mapping of odourant-induced Zif268 expression. *Eur J Neurosci* **15**:1563–74.
469 doi:10.1046/j.1460-9568.2002.01991.x
470 Ito J, Roy S, Liu Y, Cao Y, Fletcher M, Lu L, Boughter JD, Grün S, Heck DH. 2014. Whisker
471 barrel cortex delta oscillations and gamma power in the awake mouse are linked to
472 respiration. *Nat Commun* **5**:3572. doi:10.1038/ncomms4572
473 Johnson BA, Farahbod H, Leon M. 2005. Interactions between odorant functional group and
474 hydrocarbon structure influence activity in glomerular response modules in the rat olfactory
475 bulb. *J Comp Neurol* **483**:205–216. doi:10.1002/cne.20409
476 Johnson BA, Farahbod H, Xu Z, Saber S, Leon M. 2004. Local and global chemotopic
477 organization: general features of the glomerular representations of aliphatic odorants
478 differing in carbon number. *J Comp Neurol* **480**:234–49. doi:10.1002/cne.20335
479 Johnson BA, Leon M. 2000. Modular representations of odorants in the glomerular layer of the
480 rat olfactory bulb and the effects of stimulus concentration. *J Comp Neurol* **422**:496–509.
481 Johnson BA, Leon M. 1996. Spatial distribution of [14C]2-deoxyglucose uptake in the
482 glomerular layer of the rat olfactory bulb following early odor preference learning. *J Comp*
483 *Neurol* **376**:557–66. doi:10.1002/(SICI)1096-9861(19961223)376:4<557::AID-
484 CNE5>3.0.CO;2-0

485 Johnson BA, Woo CC, Duong H, Nguyen V, Leon M. 1995. A learned odor evokes an enhanced
486 Fos-like glomerular response in the olfactory bulb of young rats. *Brain Res* **699**:192–200.
487 Johnson BA, Woo CC, Hingco EE, Pham KL, Leon M. 1999. Multidimensional chemotopic
488 responses to n-aliphatic acid odorants in the rat olfactory bulb. *J Comp Neurol* **409**:529–48.
489 Johnson BA, Xu Z, Ali SS, Leon M. 2009. Spatial representations of odorants in olfactory bulbs
490 of rats and mice: Similarities and differences in chemotopic organization. *J Comp Neurol*
491 **514**:658–673. doi:10.1002/cne.22046
492 Johnson MA, Tsai L, Roy DS, Valenzuela DH, Mosley C, Magklara A, Lomvardas S, Liberles
493 SD, Barnea G. 2012. Neurons expressing trace amine-associated receptors project to discrete
494 glomeruli and constitute an olfactory subsystem. *Proc Natl Acad Sci* **109**:13410–13415.
495 doi:10.1073/pnas.1206724109
496 Kandel ER, Jessell TM, Schwartz JH, Siegelbaum SA, Hudspeth AJ. 2013. Principles of Neural
497 Science, Fifth Edition, Principles of Neural Science. McGraw-Hill Education.
498 Kikuta S, Fletcher ML, Homma R, Yamasoba T, Nagayama S. 2013. Odorant Response
499 Properties of Individual Neurons in an Olfactory Glomerular Module. *Neuron* **77**.
500 doi:10.1016/j.neuron.2013.01.022
501 Kimbell JS, Godo MN, Gross EA, Joyner DR, Richardson RB, Morgan KT. 1997. Computer
502 Simulation of Inspiratory Airflow in All Regions of the F344 Rat Nasal Passages. *Toxicol*
503 *Appl Pharmacol* **145**:388–398. doi:10.1006/TAAP.1997.8206
504 Kiyokage E, Pan Y-Z, Shao Z, Kobayashi K, Szabo G, Yanagawa Y, Obata K, Okano H, Toida
505 K, Puche AC, Shipley MT. 2010. Molecular Identity of Periglomerular and Short Axon
506 Cells. *J Neurosci* **30**:1185–1196. doi:10.1523/JNEUROSCI.3497-09.2010
507 Li J, Ishii T, Feinstein P, Mombaerts P. 2004. Odorant receptor gene choice is reset by nuclear

transfer from mouse olfactory sensory neurons. *Nature* **428**:393–399. doi:10.1038/nature02433

Liberles SD. 2015. Trace amine-associated receptors: Ligands, neural circuits, and behaviors. *Curr Opin Neurobiol*. doi:10.1016/j.conb.2015.01.001

Liberles SD, Buck LB. 2006. A second class of chemosensory receptors in the olfactory epithelium. *Nature* **442**:645–650. doi:10.1038/nature05066

Lockmann AL V, Laplagne DA, Leão RN, Tort ABL. 2016. A Respiration-Coupled Rhythm in the Rat Hippocampus Independent of Theta and Slow Oscillations. *J Neurosci* **36**:5338–52. doi:10.1523/JNEUROSCI.3452-15.2016

Lodovichi C, Belluscio L, Katz LC. 2003. Functional topography of connections linking mirror-symmetric maps in the mouse olfactory bulb. *Neuron* **38**:265–76.

Marks CA, Cheng K, Cummings DM, Belluscio L. 2006. Activity-dependent plasticity in the olfactory intrabulbar map. *J Neurosci* **26**:11257–66. doi:10.1523/JNEUROSCI.2805-06.2006

Miyamichi K, Amat F, Moussavi F, Wang C, Wickersham I, Wall NR, Taniguchi H, Tasic B, Huang ZJ, He Z, Callaway EM, Horowitz MA, Luo L. 2011. Cortical representations of olfactory input by trans-synaptic tracing. *Nature* **472**:191–196. doi:10.1038/nature09714

Miyamichi K, Serizawa S, Kimura HM, Sakano H. 2005. Cellular/Molecular Continuous and Overlapping Expression Domains of Odorant Receptor Genes in the Olfactory Epithelium Determine the Dorsal/Ventral Positioning of Glomeruli in the Olfactory Bulb. doi:10.1523/JNEUROSCI.0324-05.2005

Mizuguchi R, Naritsuka H, Mori K, Yoshihara Y, Klein WH, Yoshihara Y. 2012. Tbr2 Deficiency in Mitral and Tufted Cells Disrupts Excitatory-Inhibitory Balance of Neural

Circuitry in the Mouse Olfactory Bulb. *J Neurosci* **32**:8831–8844. doi:10.1523/JNEUROSCI.5746-11.2012

Moberly AH, Schreck M, Bhattarai JP, Zweifel LS, Luo W, Ma M. 2018. Olfactory inputs modulate respiration-related rhythmic activity in the prefrontal cortex and freezing behavior. *Nat Commun* **9**:1528. doi:10.1038/s41467-018-03988-1

Mombaerts P, Wang F, Dulac C, Chao SK, Nemes A, Mendelsohn M, Edmondson J, Axel R. 1996. Visualizing an olfactory sensory map. *Cell* **87**:675–86.

Mori K, Takahashi YK, Igarashi KM, Yamaguchi M. 2006. Maps of Odorant Molecular Features in the Mammalian Olfactory Bulb. *Physiol Rev* **86**:409–433. doi:10.1152/physrev.00021.2005

Nagai Y, Sano H, Yokoi M. 2005. Transgenic expression of Cre recombinase in mitral/tufted cells of the olfactory bulb. *Genesis* **43**:12–6. doi:10.1002/gene.20146

Nagao H, Yamaguchi M, Takahash Y, Mori K. 2002. Grouping and representation of odorant receptors in domains of the olfactory bulb sensory map. *Microsc Res Tech* **58**:168–75. doi:10.1002/jemt.10146

Nagao H, Yoshihara Y, Mitsui S, Fujisawa H, Mori K. 2000. Two mirror-image sensory maps with domain organization in the mouse main olfactory bulb. *Neuroreport* **11**:3023–7. doi:10.1097/00001756-200009110-00039

Nagayama S, Enerva A, Fletcher ML, Masurkar AV, Igarashi KM, Mori K, Chen WR. 2010. Differential axonal projection of mitral and tufted cells in the mouse main olfactory system. *Front Neural Circuits* **4**. doi:10.3389/fncir.2010.00120

Nagayama S, Zeng S, Xiong W, Fletcher ML, Masurkar A V., Davis DJ, Pieribone VA, Chen WR. 2007. In Vivo Simultaneous Tracing and Ca2+ Imaging of Local Neuronal Circuits.

554 *Neuron* **53**:789–803. doi:10.1016/j.neuron.2007.02.018

555 Nguyen Chi V, Müller C, Wolfenstetter T, Yanovsky Y, Draguhn A, Tort ABL, Brankačk J.
556 2016. Hippocampal Respiration-Driven Rhythm Distinct from Theta Oscillations in Awake
557 Mice. *J Neurosci* **36**:162–77. doi:10.1523/JNEUROSCI.2848-15.2016

558 Pacifico R, Dewan A, Cawley D, Guo C, Bozza T. 2012. An Olfactory Subsystem that Mediates
559 High-Sensitivity Detection of Volatile Amines. *Cell Rep* **2**:76–88.
560 doi:10.1016/j.celrep.2012.06.006

561 Phillips ME, Sachdev RNS, Willhite DC, Shepherd GM. 2012. Respiration drives network
562 activity and modulates synaptic and circuit processing of lateral inhibition in the olfactory
563 bulb. *J Neurosci* **32**:85–98. doi:10.1523/JNEUROSCI.4278-11.2012

564 Schindelin J, Arganda-Carreras I, Frise E, Kaynig V, Longair M, Pietzsch T, Preibisch S,
565 Rueden C, Saalfeld S, Schmid B, Tinevez J-Y, White DJ, Hartenstein V, Eliceiri K,
566 Tomancak P, Cardona A. 2012. Fiji: an open-source platform for biological-image analysis.
567 *Nat Methods* **9**:676–82. doi:10.1038/nmeth.2019

568 Schoenfeld TA, Cleland TA. 2006. Anatomical Contributions to Odorant Sampling and
569 Representation in Rodents: Zoning in on Sniffing Behavior. *Chem Senses* **31**:131–144.
570 doi:10.1093/chemse/bjj015

571 Schoenfeld TA, Marchand JE, Macrides F. 1985. Topographic organization of tufted cell axonal
572 projections in the hamster main olfactory bulb: An intrabulbar associational system. *J Comp*
573 *Neurol* **235**:503–518. doi:10.1002/cne.902350408

574 Shepherd GM. 2012. Neurogastronomy : how the brain creates flavor and why it matters.
575 Columbia University Press.

576 Shusterman R, Smear MC, Koulakov AA, Rinberg D. 2011. Precise olfactory responses tile the

577 sniff cycle. *Nat Neurosci* **14**:1039–44. doi:10.1038/nn.2877

578 Sosulski DL, Bloom ML, Cutforth T, Axel R, Datta SR. 2011. Distinct representations of

579 olfactory information in different cortical centres. *Nature* **472**:213–216.

580 doi:10.1038/nature09868

581 Spors H, Grinvald A. 2002. Spatio-temporal dynamics of odor representations in the mammalian

582 olfactory bulb. *Neuron* **34**:301–15.

583 Svoboda K, Helmchen F, Denk W, Tank DW. 1999. Spread of dendritic excitation in layer 2/3

584 pyramidal neurons in rat barrel cortex in vivo. *Nat Neurosci* **2**:65–73. doi:10.1038/4569

585 Taniguchi H, He M, Wu P, Kim S, Paik R, Sugino K, Kvitsiani D, Kvitsani D, Fu Y, Lu J, Lin

586 Y, Miyoshi G, Shima Y, Fishell G, Nelson SB, Huang ZJ. 2011. A resource of Cre driver

587 lines for genetic targeting of GABAergic neurons in cerebral cortex. *Neuron* **71**:995–1013.

588 doi:10.1016/j.neuron.2011.07.026

589 Taniguchi M, Nagao H, Takahashi YK, Yamaguchi M, Mitsui S, Yagi T, Mori K, Shimizu T.

590 2003. Distorted odor maps in the olfactory bulb of semaphorin 3A-deficient mice. *J*

591 *Neurosci* **23**:1390–7.

592 Tian L, Hires SA, Mao T, Huber D, Chiappe ME, Chalasani SH, Petreanu L, Akerboom J,

593 McKinney SA, Schreiter ER, Bargmann CI, Jayaraman V, Svoboda K, Looger LL. 2009.

594 Imaging neural activity in worms, flies and mice with improved GCaMP calcium indicators.

595 *Nat Methods* **6**:875–881. doi:10.1038/nmeth.1398

596 Uchida N, Poo C, Haddad R. 2014. Coding and Transformations in the Olfactory System. *Annu*

597 *Rev Neurosci* **37**:363–385. doi:10.1146/annurev-neuro-071013-013941

598 Wachowiak M, Economo MN, Diaz-Quesada M, Brunert D, Wesson DW, White JA, Rothermel

599 M. 2013. Optical Dissection of Odor Information Processing In Vivo Using GCaMPs

600 Expressed in Specified Cell Types of the Olfactory Bulb. *J Neurosci* **33**:5285–5300.
601 doi:10.1523/JNEUROSCI.4824-12.2013
602 Wilson RI, Mainen ZF. 2006. EARLY EVENTS IN OLFACTORY PROCESSING. *Annu Rev*
603 *Neurosci* **29**:163–201. doi:10.1146/annurev.neuro.29.051605.112950
604 Yan Z, Tan J, Qin C, Lu Y, Ding C, Luo M. 2008. Precise circuitry links bilaterally symmetric
605 olfactory maps. *Neuron* **58**:613–24. doi:10.1016/j.neuron.2008.03.012
606 Yanovsky Y, Ciatipis M, Draguhn A, Tort ABL, Branka k J. 2014. Slow Oscillations in the
607 Mouse Hippocampus Entrained by Nasal Respiration. *J Neurosci* **34**:5949–5964.
608 doi:10.1523/JNEUROSCI.5287-13.2014
609 Zapiec B, Mombaerts P. 2015. Multiplex assessment of the positions of odorant receptor-specific
610 glomeruli in the mouse olfactory bulb by serial two-photon tomography. *PNAS*
611 **112**:E58732–82. doi:10.1073/pnas.1512135112
612 Zariwala HA, Borghuis BG, Hoogland TM, Madisen L, Tian L, De Zeeuw CI, Zeng H, Looger
613 LL, Svoboda K, Chen T-W. 2012. A Cre-dependent GCaMP3 reporter mouse for neuronal
614 imaging in vivo. *J Neurosci* **32**:3131–41. doi:10.1523/JNEUROSCI.4469-11.2012
615 Zhang J, Pacifico R, Cawley D, Feinstein P, Bozza T. 2013. Ultrasensitive Detection of Amines
616 by a Trace Amine-Associated Receptor. *J Neurosci* **33**:3228–3239.
617 doi:10.1523/JNEUROSCI.4299-12.2013
618 Zhao K, Dalton P, Yang GC, Scherer PW. 2006. Numerical Modeling of Turbulent and Laminar
619 Airflow and Odorant Transport during Sniffing in the Human and Rat Nose. *Chem Senses*
620 **31**:107–118. doi:10.1093/chemse/bjj008
621 Zhou Z, Belluscio L. 2012. Coding odorant concentration through activation timing between the
622 medial and lateral olfactory bulb. *Cell Rep* **2**:1143–50. doi:10.1016/j.celrep.2012.09.035

623 Zhou Z, Belluscio L. 2008. Intrabulbar projecting external tufted cells mediate a timing-based
624 mechanism that dynamically gates olfactory bulb output. *J Neurosci* **28**:9920–8.
625 doi:10.1523/JNEUROSCI.3082-08.2008
626